# Structural integrity assessment of a full-scale adhesively-bonded bi-material joint for maritime applications

Saeedifar, Milad; Saleh, Mohamed Nasr; Krairi, Anouar; de Freitas, Sofia Teixeira; Zarouchas, Dimitrios

**DOI**
10.1016/j.tws.2022.110487

**Publication date**
2023

**Document Version**
Final published version

**Published in**
Thin-Walled Structures

Thin-Walled Structures 184 (2023) 110487

Contents lists available at ScienceDirect

Thin-Walled Structures

journal homepage: www.elsevier.com/locate/tws

# Structural integrity assessment of a full-scale adhesively-bonded bi-material joint for maritime applications

Milad Saeedifar [a,*], Mohamed Nasr Saleh [a,b], Anouar Krairi [c], Sofia Teixeira de Freitas [a], Dimitrios Zarouchas [d]

[a] Faculty of Aerospace Engineering, Structural Integrity & Composites, Delft University of Technology, Delft, 2628 CD, The Netherlands
[b] Advanced Materials Research Center, Technology Innovation Institute, Masdar City, Abu Dhabi, United Arab Emirates
[c] Materials innovation institute (M2i), The Netherlands
[d] Center of Excellence in Artificial Intelligence for Structures, Aerospace Engineering Faculty, Delft University of Technology, The Netherlands

ARTICLE INFO

*Keywords:*
Adhesively-bonded bi-material joint
Structural health monitoring
Full-scale mechanical test
Finite element analysis (FEA)
Acoustic emission
Integrity assessment

ABSTRACT

The present study proposes a comprehensive integrity assessment approach for a full-scale adhesively-bonded bi-material joint for maritime applications. The joint represents a cross-section of the bond-line connection of a ship with a steel hull and a sandwich composite superstructure. The full-scale joint consists of a sandwich composite core adhesively bonded to two U-shaped steel brackets. The joint was subjected to a quasi-static loading profile including 6 load cycles up to the final failure. Each load cycle was followed by a dwell segment holding the joint at the maximum displacement for 30 s and then unloading to 50% of the maximum displacement. Three Structural Health Monitoring (SHM) techniques including Acoustic Emission (AE), Fiber Optic Sensor (FOS), and Digital Image Correlation (DIC) were employed during the test to assess the damage state of the joint. Moreover, a Finite Element Model (FEM) was developed to simulate the evolution behavior of different damage mechanisms in the joint and the FE results were compared against the experimental findings. The obtained results showed that the integration of all the employed techniques could successfully detect the damage initiation, assess the severity of the damage, localize the critical regions of the joint, and distinguish the different damage mechanisms.

## 1. Introduction

Traditionally, the shipbuilding industry has focused for decades mainly on using steel-based structures and components. This always raised concerns regarding weight, environmental impact, carbon footprint and the interaction between such components and the maritime environment leading to corrosion for instance [1]. All these aspects translate directly into additional energy consumption and associated costs. Thanks to the emerging developments in the composite materials industry, more attention has been given towards utilizing such lightweight, yet stiff and strong, materials in marine structures. This transition provides the marine sector with several benefits [2,3], however to date, the application of these materials is restricted only for secondary structures, whose failure is not detrimental to the structural safety. With the use of dissimilar materials (steel and composites) in shipbuilding, alternative joining techniques are essential. Adhesive bonding is introduced as an alternative solution that can offer the capability of joining dissimilar materials at no extra weight cost while not compromising the structural integrity [3,4]. However, because of the complexity of these joints, they are susceptible to complex damage modes including adherends failure, adhesive failure, and cohesive failure. This requires smart and robust structural health monitoring (SHM) systems to be put in place to always monitor the structural integrity and provide sufficient information and data about the state of such adhesively bonded joints in service.

Comprehensive integrity assessment of a full-scale structure is usually done in a couple of steps to reveal: (a) if there is any damage in the structure, (b) where the location of the damage is, (c) how much severe the damage is, and (d) what the type of the damage is. Usually, an SHM technique cannot satisfy all of these levels solely, while by combining and fusing the results obtained from different SHM techniques the integrity state of the structure can be evaluated comprehensively. Among all the SHM techniques, Acoustic Emission (AE) has been widely used for the damage detection and classification in hybrid structures [5–8]. Digital Image Correlation (DIC) and Fiber Optic Sensor (FOS) are other SHM techniques that have shown good capabilities for strain measurement in the structures [9–13]. Analyzing this strain data can provide valuable information regarding the damage state of the structure. Saeedifar et al. and Saleh et al. [14,15] used the AE to detect the damage initiation in the bi-material double-lap

* Corresponding author.
*E-mail address:* m_saeedi@sbu.ac.ir (M. Saeedifar).

https://doi.org/10.1016/j.tws.2022.110487
Received 24 September 2022; Received in revised form 14 December 2022; Accepted 19 December 2022
Available online xxxx

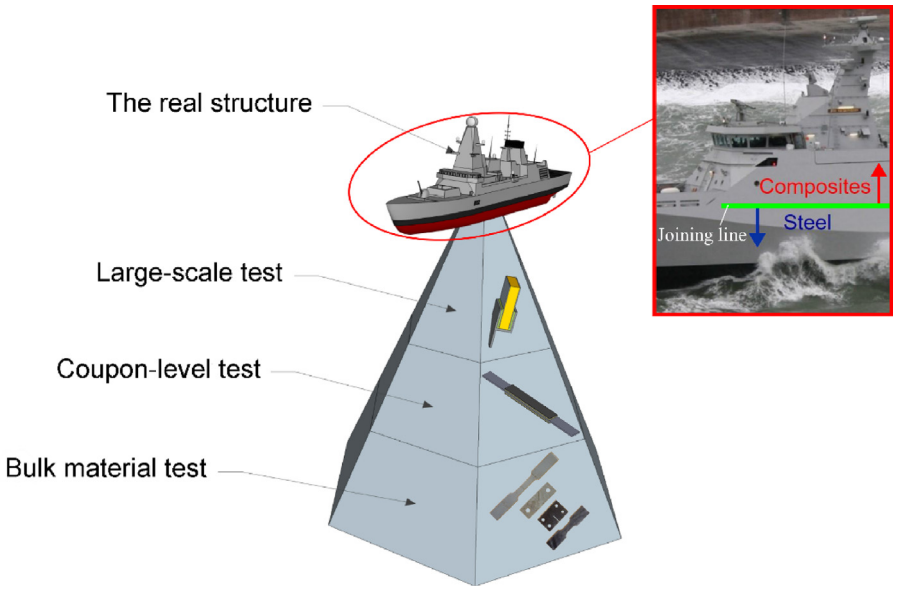


**Fig. 1.** The proposed test pyramid for the QUALIFY project.

joint coupons. They detected the damage initiation and also tracked the damage evolution in the joints. In addition, they used a supervised classifier to distinguish different damage mechanisms based on their AE signal features. The AE results were then compared to the FOS and DIC findings. Xu et al. [16,17] investigated the effect of joint geometry on the damage of a bolted hybrid fiber metal laminate (FML) joint using AE and DIC. The proposed method could track the damage initiation and propagation within the composite layer and it could also capture the strain field on the surface of the joint. Dia et al. [18] classified different damage mechanisms of a metal-composite bi-material laminate by analyzing the AE data using the unsupervised clustering and supervised classification methods. Saeedifar et al. [7] used the AE to assess the damage state of a titanium skin adhesively bonded to CFRP stiffeners. They detected the damage initiation and also identified the different damage types using the particle swarm optimization clustering method.

The aforementioned literature was conducted at coupon-level tests, while there are serious concerns regarding the implementation of the obtained results from the coupon-level tests to the full-scale structure. This is because of the complex geometry and larger size of the real structure that leads to increasing wave attenuation, larger strain and load levels, and finally, complex interference of damage mechanisms in the full-scale structures.

The present study is a follow-up to the previous work by the group [14,15] which was dedicated to the integrity assessment of a double-lap bi-material adhesively bonded joint. These series of works are part of the international project, QUALIFY, funded by Interreg2Seas Mers Zeeën, focusing on providing qualification guidelines for large-scale adhesively bonded joints for lightweight and safe maritime transport. The main scope of the two previous studies was to establish and verify an SHM system based on the constituent materials and coupon level tests (see Fig. 1). In the present study, the effectiveness of the proposed SHM system to monitor the integrity of the real large-scale joint is tested and evaluated.

## 2. Materials and manufacturing

The full-scale joint is depicted in Fig. 2. It represents a segment along the joining line of the steel hull and the sandwich composite superstructure in the real ship. For producing the joint in actual shipyard

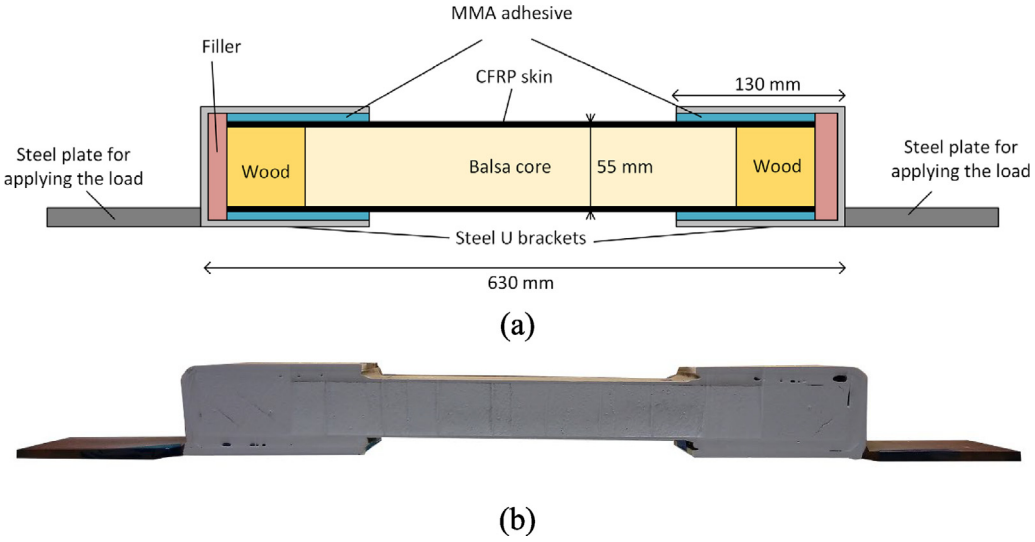


**Fig. 2.** (a) A schematic of the full-scale joint, and (b) the real view of the joint.

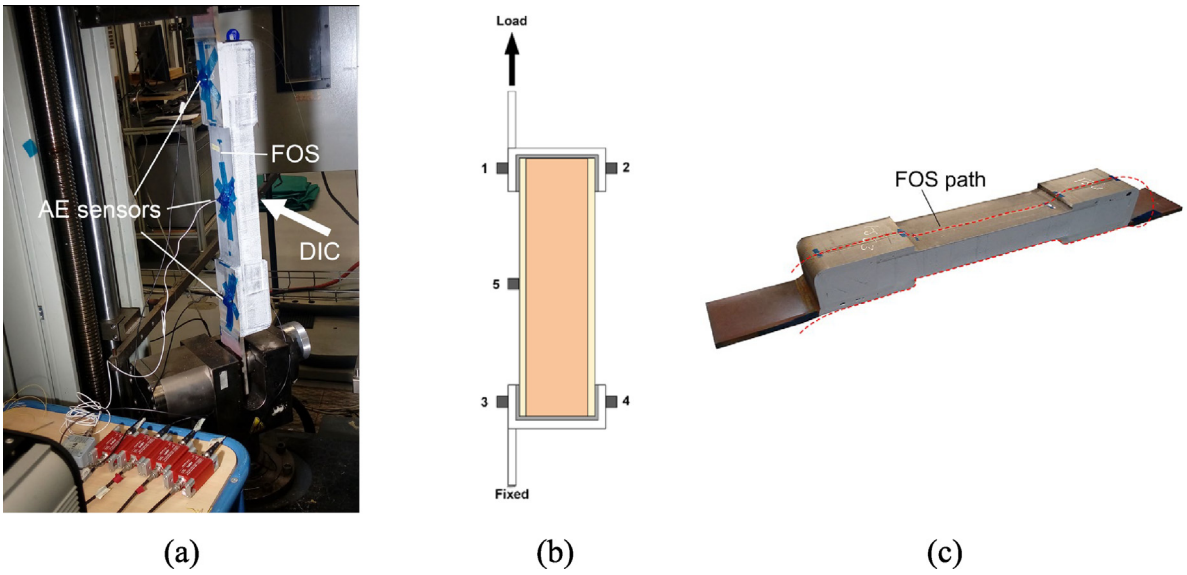


**Fig. 3.** (a) The quasi-static tensile test setup, (b) the arrangement of the AE sensors on the joint, and (c) the FOS path on both sides of the joint.

conditions (Damen Schelde Naval Shipbuilding, the Netherlands), two ends of a large sandwich panel were placed between two U-shaped steel brackets (shipbuilding steel AH36). The sandwich section was made of a balsa core with two carbon-fiber reinforced polymer (CFRP) skins with a quasi-isotropic layup. A gap of ~10 mm between the sandwich panel and steel brackets was filled with a two-component methyl methacrylate (MMA) adhesive which provides high toughness to the joint. The injection of the MMA followed the best standard practice provided by the industrial partners to mimic the real manufacturing conditions. Two wooden blocks were placed next to the balsa core at two ends of the sandwich panel, and the gap between the bottom of the steel bracket and the wooden block was filled with a filler material. This was mainly done to avoid the formation of a butt joint at the end of the specimen which could trigger damage initiation at that location, as the focus of the test was the overlap shear performance. For the loading of the joint, a steel flange with a larger thickness (12 mm) was welded to the two U-shaped steel brackets.

## 3. Experimental procedures

### 3.1. Mechanical tensile testing

The joint was subjected to a quasi-static loading profile, including 6 loading cycles up to the final failure using a 250 kN universal tension/compression Zwick machine. The loading profile consists of five loading cycles up to 1.1, 2.2, 3.3, 4.4, and 5.5 mm of the crosshead displacement respectively, followed by the 6th loading cycle up to the final failure. In each loading cycle, once the displacement reached the predefined maximum displacement of that cycle, the joint was held at that displacement level for 30 s, and then the displacement decreased with the same crosshead rate to 50% of the maximum displacement of that cycle. The test was performed under the displacement-control mode with a crosshead rate of 0.75 mm/min. As depicted in Fig. 3(a), the SHM techniques of AE, DIC, FOS, and visual inspection were used to identify the damage in the full-scale joint during the tensile test. Five AE sensors, placed at pre-defined positions on the joint surface, captured AE signals during the tensile test. The arrangement of the AE sensors is depicted in Fig. 3(b). Accordingly, two sensors were placed on both sides of the upper steel bracket (sensors 1 and 2), and one on the CFRP skin at mid-height of the joint (sensor 5). The last two sensors were placed on both sides of the lower steel bracket (sensors 3 and 4). The DIC cameras, located at the front side of the joint, took a picture from the top and bottom parts of the joint every 3 s. The FOS was attached to both lateral sides of the joint along the longitudinal direction to record the longitudinal strain experienced by the joint during the tensile test. The path of the FOS on the lateral sides of the joint is visible in Fig. 3(c).

### 3.2. Acoustic Emission (AE)

The AE events generated during the tensile loading of the full-scale joint were recorded by the five broad-band AE sensors, AE1045SVS900M from Vallen Systeme GmbH, with external 34 dB pre-amplifiers. The operating frequency of the sensors is 100–900 kHz. The AE hits were recorded by an AMSY-6 Vallen 8-channel AE system. The sampling rate was 2 MHz, and the threshold was set at 50 dB, similar to the coupon-level tests. This threshold level was chosen due to the fact that for a real ship in operation, because of the high environmental noises coming from the propulsion system, electronic devices, structural vibrations, etc., setting a low threshold can lead to capturing too many noisy signals. A standard pencil lead breakage test [19] was performed before the tensile test to check the reproducibility of the AE sensors.

### 3.3. Digital Image Correlation (DIC)

Two-dimensional (2D) DIC was used to visualize the strain contour map on the surface of both the top and bottom connections of the full-scale joint (see Fig. 3). The DIC system consisted of two 9MP cameras, equipped with a "XENOPLAN 1.4/23" lens. The speckle pattern images were captured and recorded using ViC-Snap 8 software, a product of "Correlated Solutions Inc.". The DIC system was synchronized with the testing machine using a two-channel analog connection for the applied displacement and measured force respectively. The used acquisition rate was 0.2 frames per second (fps). The captured images by ViC-Snap 8 were then post-processed using ViC-2D 6 software. For the processing, the subset size was set to 75 × 75 pixels with a step size (distance between subsets) of 20 pixels. An observation window of (135 × 256) $mm^2$ resulted in an image with dimensions of (2160 × 4096) pixels.

### 3.4. Fiber Optic Sensor (FOS)

An optical fiber connected to the OBR ODiSI-B interrogator, from Luna Innovations Inc., was used to measure the longitudinal strain of the joint. The interrogator measures the strain by capturing and processing the Rayleigh backscatter radiations. The optical fiber consists of three sections: (1) LC/APC connector, (2) the measuring section,


**Fig. 4.** The FE model for tensile tests. The loading is applied in the gripping region.

**Table 1**
Summary of the bulk material properties.

| | |
|---|---|
| Adhesive | Young's modulus: $E = 242 \pm 20$ MPa and Poisson's ratio: $\nu = 0.42$<br>Hill's yielding function is defined by<br>$F(\sigma_{22}-\sigma_{33})^2 + G(\sigma_{33}-\sigma_{11})^2 + H(\sigma_{11}-\sigma_{22})^2 + 2L\sigma_{23}^2 + 2M\sigma_{31}^2 + 2N\sigma_{12}^2 = 1$<br>With $F = G = H = 1/\sigma_y^n$ $L = M = N = 1.9/\sigma_y^n$. Given $\sigma_y^n$ as the yield limit under tensile/compression loadings |
| Composite | In-plane tensile modulus: 36 GPa, Shear modulus: 13.7 GPa |
| Steel | Young's modulus: 206 GPa, Elastic yield limit: 355 MPa |
| Balsa | Tensile modulus perpendicular to the plane: 2791 MPa and a shear modulus: 187 MPa |

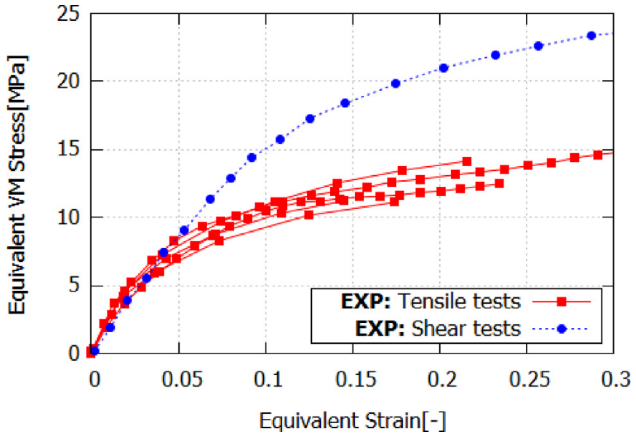


**Fig. 5.** Comparison between the response of adhesive under shear and tensile loadings. The equivalent stress $\sigma_e = \tau\sqrt{3}$ and equivalent strain $\varepsilon_e = \frac{\gamma}{\sqrt{3}}$.

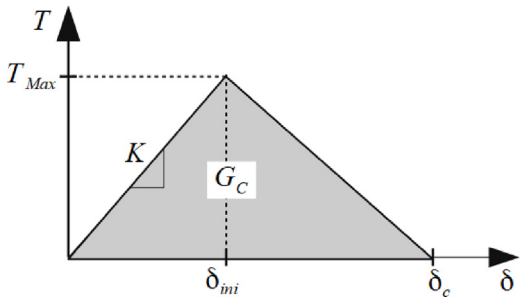


**Fig. 6.** Graphical representation of the bilinear cohesive law: $G_C$ is the critical fracture energy, $T_{Max}$ is the maximum traction, $K$ is the initial stiffness, $\delta_{ini}$ and $\delta_c$ correspond respectively to the initial and the critical separation values.

Graded-Index Multimode (GIMM) fiber from Plasma Optical Fibre Inc., and (3) a coreless section spliced to the end of the measuring section, from THORLABS Inc., to reduce the noise level of the measurements. The spatial resolution of the strains was 0.65 mm, and the sampling rate was 23.8 Hz.

## 4. FE simulations

The joint was modeled as a 3D model using the Finite element (FE) method with the commercial software, ABAQUS®2020 (see Fig. 4). The FE simulations were used to provide a better understanding of the obtained experimental results by the different techniques. The solids were meshed with second-order hexahedral continuum elements (C3D20) wherever possible, especially for the adhesive layers, to accurately capture the material shear behavior. For the composite panels, continuum shell elements (SC8R) were used to also improve the computational efficiency.

Several modeling assumptions were considered for the behavior of the bulk materials and the different interfaces. For modeling the nonlinear behavior of the used adhesive, an elastoplastic constitutive behavior model is used. To choose the yielding criteria, the adhesive responses under the tensile and the shear loadings were compared using the Von Mises (VM) equivalent stress in Fig. 5. The comparison shows a stronger material response under shear loading compared to the tensile loading using VM equivalent stress. From the modeling point of view, this will forbid the VM criteria to be used as a yielding criterion, requiring instead an anisotropic yielding criterion such as Hill's yielding criterion [20] to describe the adhesive behavior. A reminder of the yielding function expression is given in Table 1.

The quasi-isotropic composite panels are assumed to be composed of transverse isotropic elastic plies. Steel parts are modeled as an elastoplastic material, to consider possible yielding, and the balsa wood is assumed to have an isotropic elastic behavior. A summary of the used material properties for the different constituents is given in Table 1.

The different interfaces (i.e., steel to adhesive and adhesive to composite) are modeled using bilinear cohesive laws (see Fig. 6 for illustration). The mode-mixity is considered using a power law with a coefficient of 1.

The cohesive law for the steel to adhesive was calibrated using TAST tests (see paper [21] for details of the tests) and DCB test. In both types of tests, the selected adhesive layer thickness was 8 to 10 mm corresponding to the thickness used in the joint. For the interfaces between the adhesive and the composite, a DCB test was performed and used to calibrate the cohesive law. Skin failure of the composite was observed as the main failure mechanism of the joint. Since the shear fracture mode (Mode II) test was difficult to perform in the case of composite substrates, it was assumed that the corresponding material parameters for the cohesive law are the same as the ones obtained from the DCB test (Mode I). This simplification is expected to give a

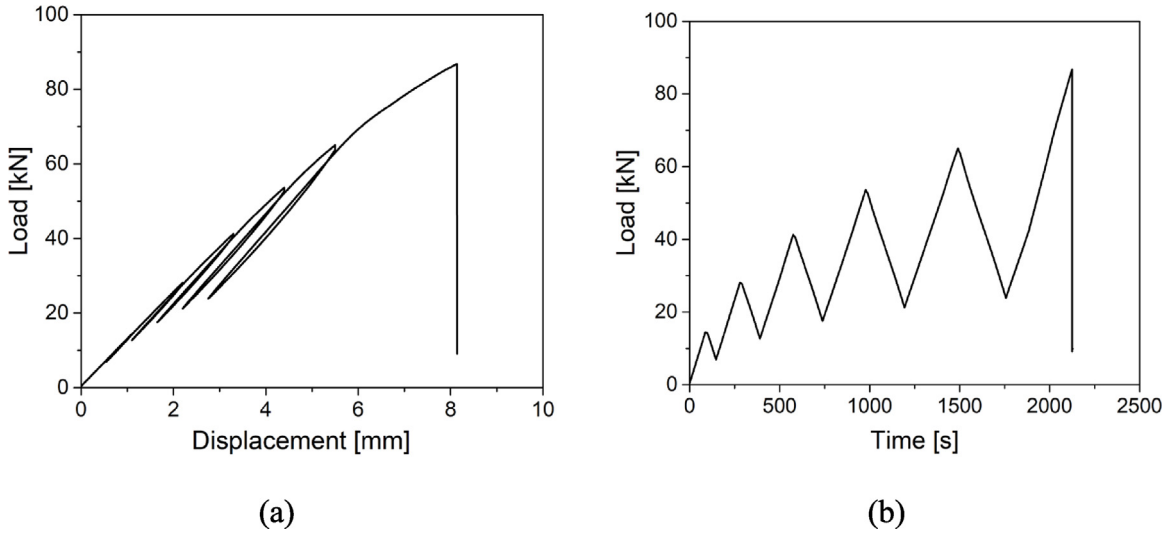


**Fig. 7.** (a) The load–displacement curve, and (b) load–time curve of the joint.

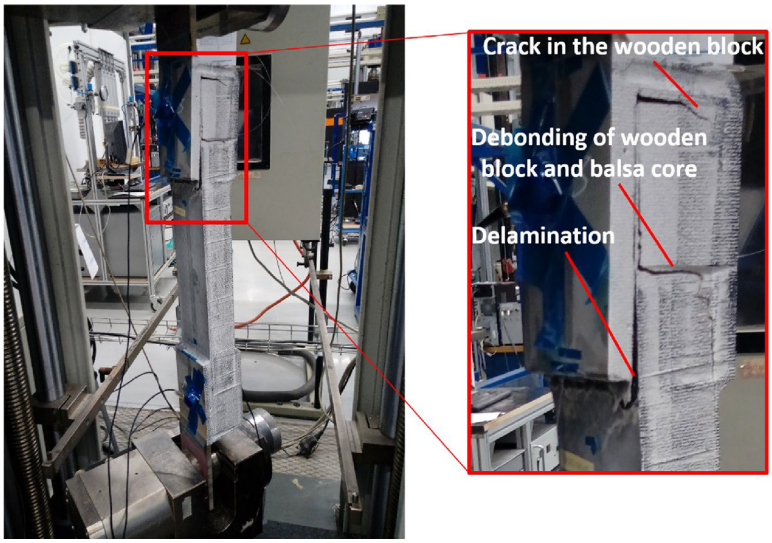


**Fig. 8.** The final failure mode of the joint.

conservative estimation of the joint failure under some loading cases especially if the fracture Mode II is dominant. For both the TAST and the DCB tests, FE models were built to simulate the tests, and the material parameters for the cohesive law were obtained by reverse engineering. The used material parameters for the different cohesive laws are given in Table 2.

## 5. Results and discussion

### 5.1. Experimental results

The load–displacement and load–time curves of the joint are depicted in Fig. 7. The maximum load of the joint was 86.8 kN.

The image of the final failure of the joint is shown in Fig. 8. The joint failed close to the upper steel bracket because of large delamination within the CFRP skin. The delamination is followed by the damage in the wooden block next to the balsa core. The damage in the wooden block is not further investigated hereafter because as already stated, the wooden blocks were auxiliary components in the tested joint. Experimental observations revealed that the joint failed because of the induced bending in the joint, which refers to the asymmetry of the joint under loading conditions to mimic the real-life loading condition of the joint. The measured strain by the FOS clearly indicates the bending induced at the CFRP skin of the joint (see Fig. 9). As it is clear, there is a large tension strain at the left CFRP skin (Section 2), while the right CFRP skin is under a compression strain (Section 5). Finally, the joint failed at the side which is under tension stress (see Fig. 9).

The cumulative number of AE events recorded by the five AE sensors is depicted in Fig. 10. As it is clear, the first significant AE activities of the joint started in the 2nd load cycle (at a load of ~22.5 kN). These AE activities show the damage initiation in the joint. By comparing the corresponding load to the initiation of the AE activities to the final fracture load (22.5 kN vs. 86.5 kN), it is revealed that the AE detected the early-stage damage in the joint at a load of ~25% of the final fracture load. The AE curve shows a step-by-step increasing trend that indicates the progressive damage in the joint. According to

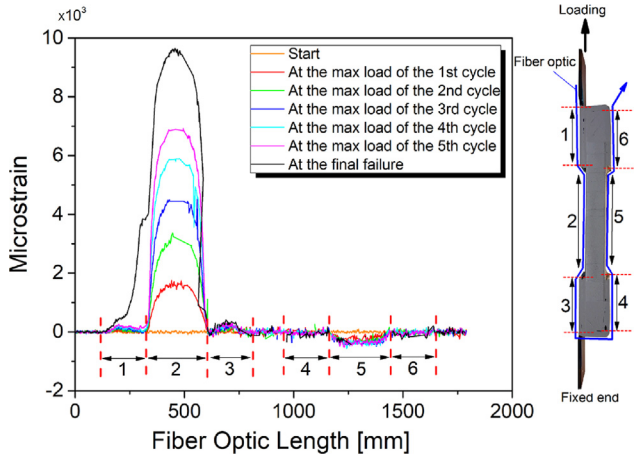


**Fig. 9.** The FOS longitudinal strain distribution in the joint.

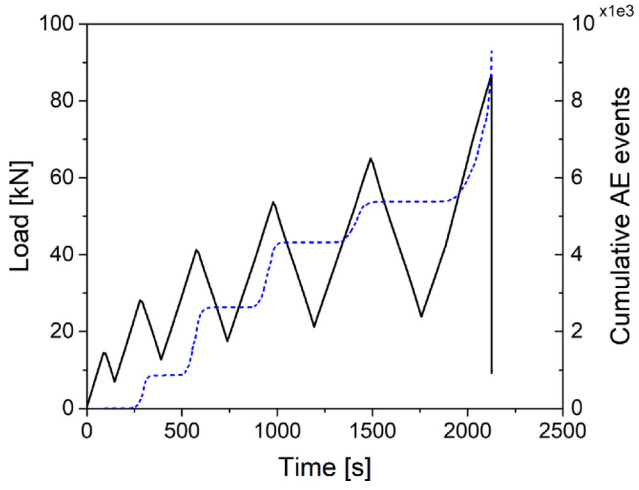


**Fig. 10.** Cumulative AE events curve of the joint.

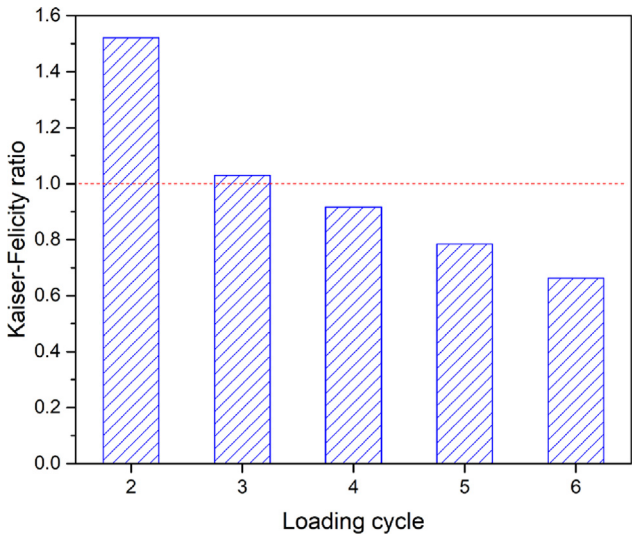


**Fig. 11.** Kaiser and Felicity ratios for the joint.

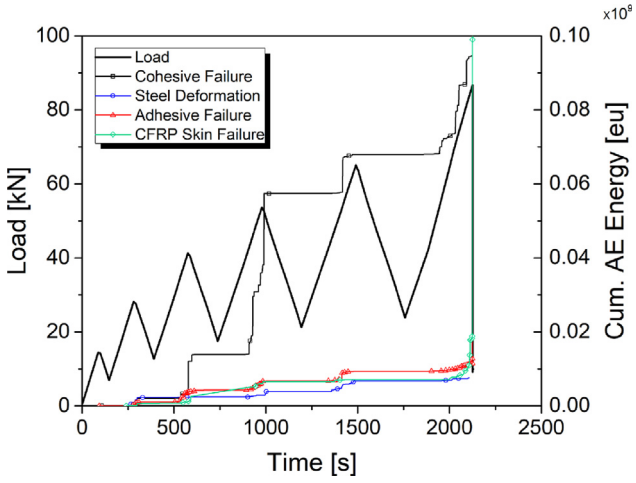


**Fig. 12.** The cumulative AE energy curve of the different damage mechanisms of the joint.

the AE profile of the first load cycles, the AE curve is plateau during the unloading phase. In the next reloading phase, as long as the load level is less than the maximum load of the previous load cycle, the AE curve is still plateau, while once the load crosses the maximum load of the previous load cycle, the cumulative number of AE events increases. This phenomenon is called the Kaiser effect that shows the joint is still healthy. During the reloading phase, if the AE activities increase at load levels less than the maximum load of the previous load cycle, it indicates the occurrence of the critical damage in the joint that adversely affected the integrity of the joint. This phenomenon is named Felicity effect [7,22] and it can be seen for the last load cycles. If the load corresponding to the initiation of the new AE activities in the reloading phase is divided by the maximum load of the previous load cycle, it can be used as an indication of Kaiser or Felicity effects [7,22]. The index larger than or equal to 1 indicates the Kaiser effect, while the index smaller than 1 indicates the Felicity effect. This index is depicted in Fig. 11 for the joint. As it is clear, the Felicity effect is obvious at the 4th load cycle. This indicates that the critical damage of the joint started in the 4th load cycle. The load level corresponds to the critical damage detected by the AE is ~65% of the final fracture load which offers a good margin for reacting to damage once captured by the AE by conducting corrective actions in real life applications via maintenance or repair to avoid the catastrophic final failure. Therefore, as a summary, the AE could detect the damage initiation and assess the severity of the damage in the full-scale joint.

**Table 2**
Summary of the material properties for the cohesive laws.

| | |
|---|---|
| Interface steel to adhesive | Damage initiation: $T_t = 10$ MPa; $T_{s1} = T_{s2} = 16.0$ MPa<br>Damage evolution: $G_I = 1.5; G_{II} = G_{III} = 16.77$ kJ/m$^2$ |
| Interface composite to adhesive | Damage initiation: $T_t = T_{s1} = T_{s2} = 6.5$ MPa<br>Damage evolution: $G_I = G_{II} = G_{III} = 1.8$ kJ/m$^2$ |

The next step of the damage assessment of the full-scale joint is identifying the damage type. In our previous work [14], an ensemble-bagged-tree supervised classifier was developed to classify the damage mechanisms of the standard double-lap joint coupons. The model was first trained by the AE data collected from the tests of the constituent materials of the joint. The AE signals of the four damage mechanisms,

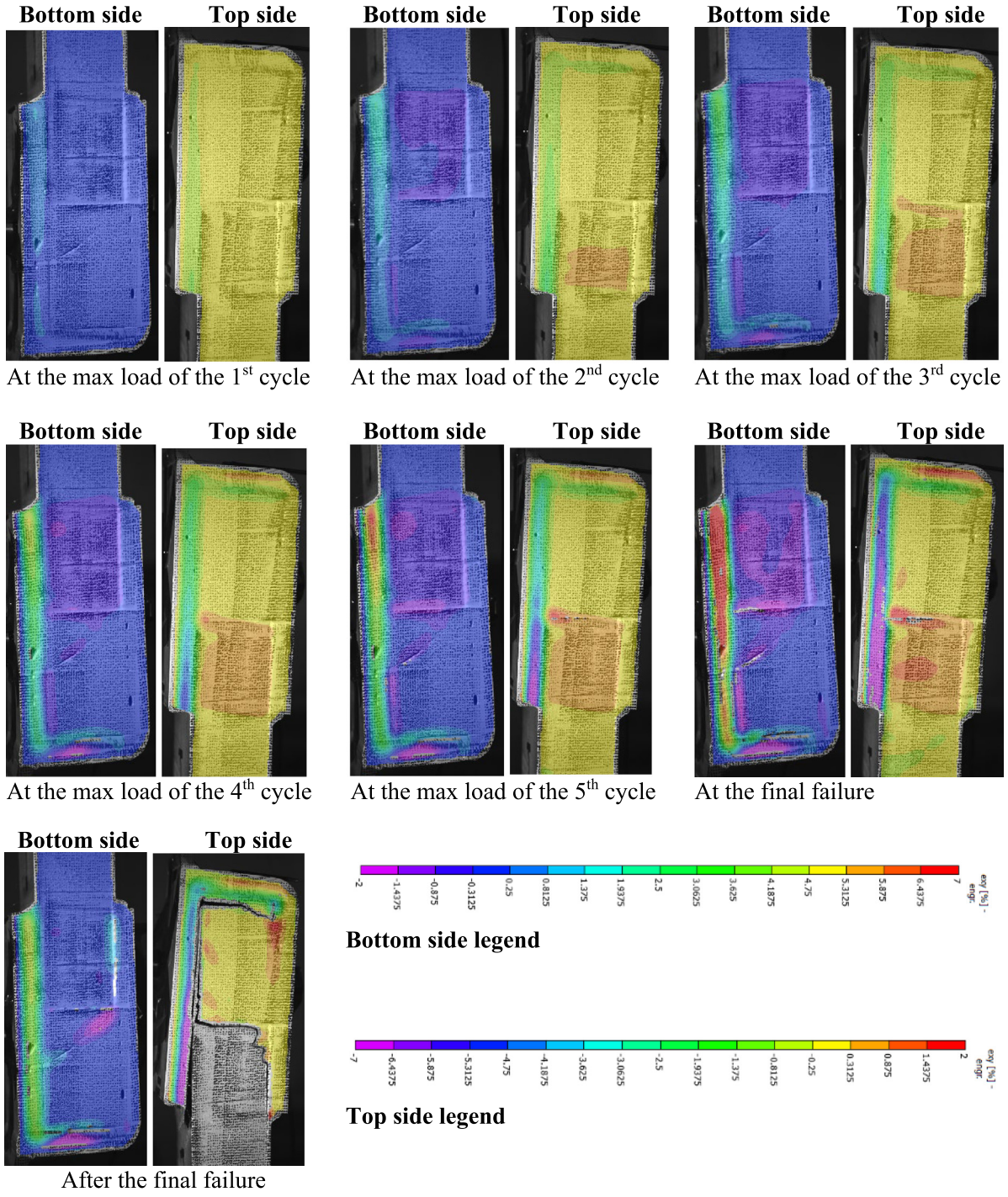


**Fig. 13.** Shear strain contours of the top and bottom parts of the joint during the tensile loading.

including cohesive failure, adhesive failure, steel deformation, and CFRP skin failure were collected from the fracture tests of the adhesive material, fracture tests of adhesively bonded steel-to-steel and CFRP-to-CFRP DCB specimens, tensile and shear tests of steel, and tensile tests of CFRP skin material, respectively. Eight appropriate AE features were extracted for each AE signal and the classifier was trained by the labeled AE data. Afterward, the classifier was used to classify different damage mechanisms in the Double-Lap Joint (DLJ) coupons made of the same constituent materials. The classified damages by the AE were consistent with the damages observed in the DLJ visually.

In order to upscale the results and apply them to the full-scale level, the developed classifier is used here to classify different damage mechanisms of the full-scale joint. Therefore, the same eight AE features, which were used for training the classifier, i.e., amplitude, rise time, duration, counts, energy, RMS, centroid frequency, and peak frequency,

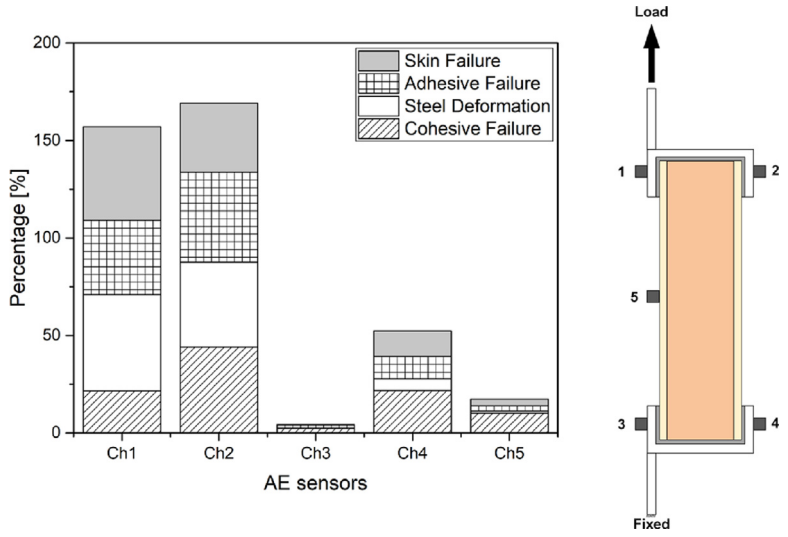


**Fig. 14.** The contribution of different damage mechanisms per each AE sensor for the joint.

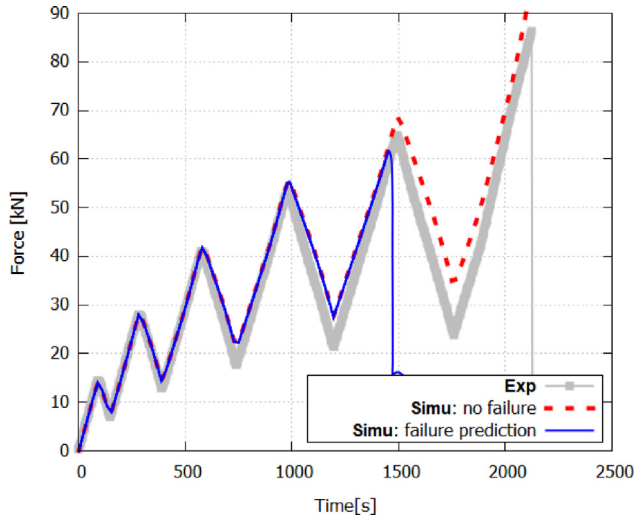


**Fig. 15.** Comparison between the force predicted by the FE simulations and the measured experimental values for the joint.

are extracted for the full-scale joint's AE signals. Then, this data is fed into the classifier to be labeled and classified.

The cumulative AE energy curves of the classified AE signals are depicted in Fig. 12. From the progressive damage point of view, irrespective of the instantaneous jump at the end of the test (at the final failure moment), the dominant damage mechanisms are CFRP skin failure, which is obvious in Fig. 8, and shear deformation of the adhesive layer, "cohesive failure", which is obviously visible in the DIC results (see Fig. 13). These two figures indicate the shear stress distribution in the joint at the maximum load of each cycle. As it is obvious, by increasing the load, a considerable plastic shear strain is formed at the adhesive layer of the joint that confirms the presence of a huge amount of cohesive failure signals in the classified AE results (see Fig. 12).

In order to specify the critical regions of the joint where most of the damages occur, the distribution of the recorded AE signals among the five AE sensors is plotted in Fig. 14. The AE sensors Ch1 and Ch2, which were close to the final failure location (top side), recorded most of the AE signals, while AE sensors Ch3 and Ch4, which were far from the final failure location, recorded a few AE signals. The AE sensor Ch5, which was located at mid-height of the joint, on the CFRP skin, recorded a few AE signals that means the damage zone is far from the middle of the joint and the critical parts of the joint are two adhesively-bonded ends of the sandwich structure.

### 5.2. FE results

The FE results are presented in this section, and they are compared against the macroscopic load–displacement curves, FOS strain data for the lateral sides of the joint, DIC strain contours on the front surface of the joint, and the classified AE data. Fig. 15 shows a comparison between the predicted forces by the FE models for joint and the experimental measurements. The stiffness of the joint is predicted well. Regarding the values of forces at failure, an underestimation of the force at failure is obtained. As already stated, this is expected because for the interface between the composite and adhesive, the CZM calibration was done using the mode I fracture energy release rate ($G_{IC}$), and $G_{IIC}$ was considered equal to $G_{IC}$, while in practice $G_{IIC}$ is higher than $G_{IC}$. Therefore, because the shear traction seems to be dominant in the joint, an underestimation of the force at failure is obtained. Regarding the dominant damage mechanisms, there is good consistency between the predicted damage modes and the damages observed in the experiments.

Fig. 16 shows the longitudinal strain on the lateral sides of the simulated joint in comparison with the true longitudinal strain measured by the FOS during the tests. Again, a good agreement is obtained for low global displacements corresponding to the first cycles, while an overestimation similar to the global response in terms of force is observed. This may also be related to possible damage in the welding between the steel flanges and the U-shaped steel parts.

Besides comparing the global strain of the joint, local strains measurements in the adhesive section obtained from the DIC are compared to the predicted strains at this section by the FE model (see Fig. 17). The comparison is done for eight points on the adhesive part of the joint, as depicted in Fig. 17. A good correlation between the experimental measurements and the FE predictions is obtained. The majority of the load seems to be carried out by one side of the joint, because of its

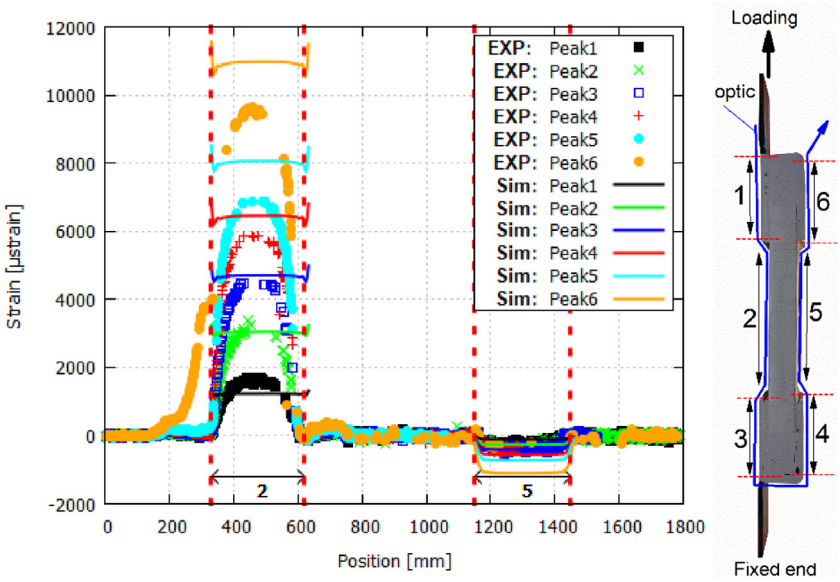


**Fig. 16.** Comparison between the predicted strains by the FE simulations and the experimental measurements obtained by FOS for the joint.

asymmetric geometry and the loading conditions imposed. The results show that the dominant strains in the adhesive are shear strains.

According to the dominant damage modes indicated by the AE results (see Figs. 12 and 14) and the visual inspection and DIC (see Figs. 8 and 13), the failure of the composite skin in contact with the adhesive part, which experiences high shear stress, is the main failure mechanism. The location of the crack initiation was also confirmed by the FE simulations as showed in Fig. 18.

The FE results were compared to the experimental results from the load–displacement curve, global strains, and local strains points of view. The predicted damage mechanisms by the FE model can be also compared to the classified damage mechanisms by the AE. To this aim, based on the FE results, the accumulated plastic deformations in critical regions of the adhesive (cohesive failure) and the steel (steel deformation), and the adhesive failure at the interface of the adhesive part to the composite near the failure initiation location, are plotted in Fig. 19. On the other hand, the cumulative AE energy for these damage mechanisms recorded by the closest AE sensor to that critical region (Ch1) is plotted and they are compared together. The average "adhesive failure" around the crack initiation location is plotted in Fig. 19(a). The value of 1 corresponds to the propagation of the crack leading to the final failure of the joint. This damage value can be correlated with the cumulative energy of "adhesive failure" AE signals.

The adhesive material around the crack initiation location experiences some plastic deformations (cohesive failure) due to the complex stress state: the combination of the shear stress and peel stress. The value of the average plastic accumulations in these regions is given in Fig. 19(b), and it is compared to the cumulative energy of "cohesive failure" AE signals.

Plastic deformations of the steel parts were also predicted by the FE model, mainly at the connection region between the U-shaped part and the flange. The plastic deformation accumulations plotted in Fig. 19(c) show similarities to the cumulative energy of "steel deformation" AE signals.

As it is clear, the general trend of the FE curves and cumulative AE energy curves is almost consistent confirming the acceptable performance of the supervised classifier. In some cases, the AE detected the damage initiation earlier than the FE model which refers to the high sensitivity of the AE technique to the micro-damages.

## 6. Conclusion

The present study was dedicated to the Structural Health Monitoring (SHM) of an adhesively bonded bi-material full-scale joint. The SHM techniques of Acoustic Emission (AE), Fiber Optic Sensor (FOS), and Digital Image Correlation (DIC) were employed to assess the integrity of the joint while it was subjected to a quasi-static load to the final failure. The results showed that AE could detect the early-stage damage in the joint at load levels around 25% of the failure load. It also determined the critical damage that significantly affected the integrity of the joint at load levels around 65% of the failure load. The supervised classifier, which was developed and verified based on the constituent materials tests and the coupon-level tests, was employed to classify the AE signals of the damage mechanisms of the full-scale joint. The classified damages were consistent with the damages observed in the fractured joint, and FOS and DIC results. In addition, a FE model was proposed to help to interpret the AE results and present a better understanding of the joint response under the applied loading conditions, and to predict the failure mechanism for the joint. There was good consistency between the results obtained from different SHM techniques and the FE results. This study showed that the integration of the employed SHM techniques could successfully monitor the integrity of the full-scale adhesively-bonded bi-material joints.

## CRediT authorship contribution statement

**Milad Saeedifar:** Writing – review & editing, Writing – original draft, Methodology, Investigation, Formal analysis, Conceptualization. **Mohamed Nasr Saleh:** Writing – review & editing, Writing – original draft, Methodology, Investigation, Formal analysis, Conceptualization. **Anouar Krairi:** Writing – review & editing, Writing – original draft, Methodology, Formal analysis. **Sofia Teixeira de Freitas:** Writing – review & editing, Writing – original draft, Supervision. **Dimitrios Zarouchas:** Writing – review & editing, Supervision.

## Declaration of competing interest

The authors declare that they have no known competing financial interests or personal relationships that could have appeared to influence the work reported in this paper.

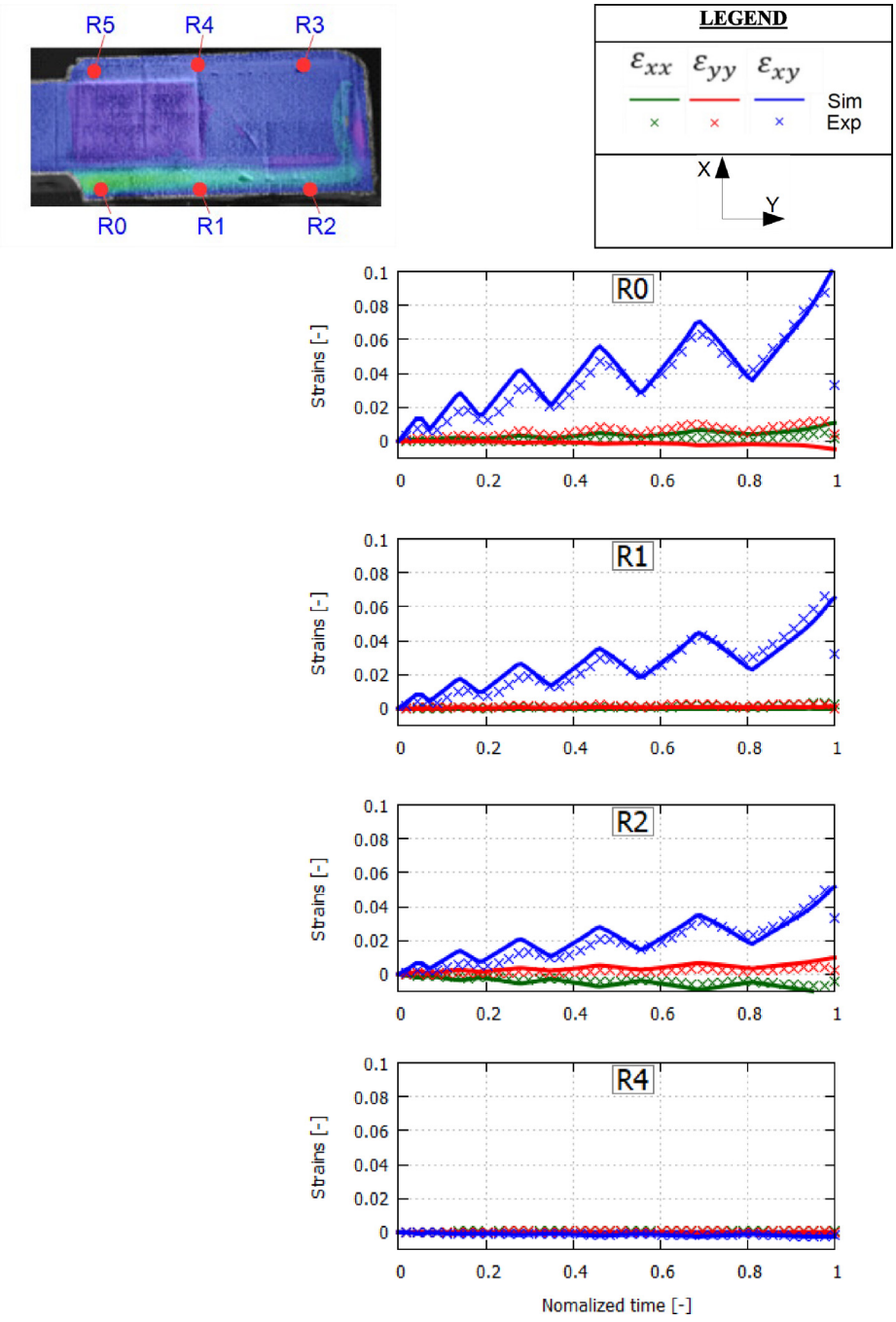


**Fig. 17.** Comparison between the predicted strains by the FE simulations and the experimental measurement obtained by DIC for the joint.

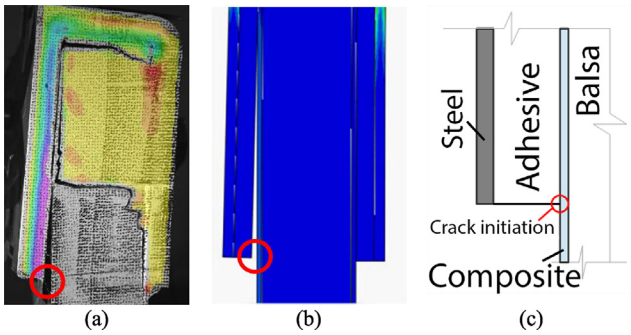


**Fig. 18.** Location of the crack initiation leading to the final failure of the joint. (a) the experimental test, (b) FE simulation prediction, and (c) graphical illustration.


## Funding

This research was carried out within the project "QUALIFY–Enabling Qualification of Hybrid Joints for Lightweight and Safe Maritime Transport (2S03-051)", co-funded by the INTERREG 2Seas Mers Zeeën program.


## Data availability

The raw/processed data required to reproduce these findings cannot be shared at this time as the data also forms part of an ongoing study.

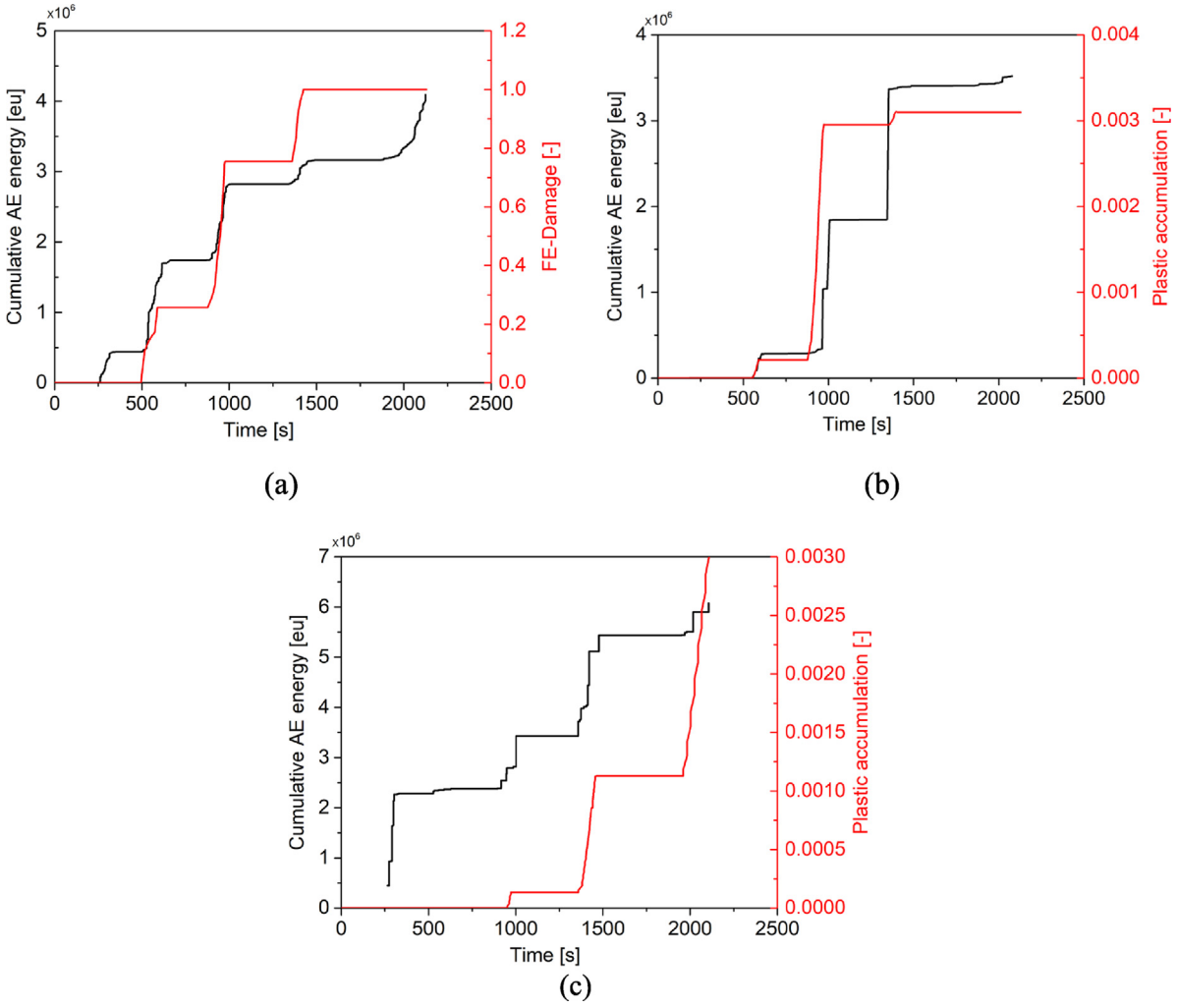


**Fig. 19.** (a) Average adhesive failure in the region around the crack initiation location of the joint, (b) average plastic accumulation in the adhesive region around the crack initiation location (cohesive failure) of the joint, and (c) average plastic accumulation in the steel around the welding region of the joint.

## References


[1] M. Mieloszyk, K. Majewska, W. Ostachowicz, Application of embedded fibre bragg grating sensors for structural health monitoring of complex composite structures for marine applications, Mar. Struct. 76 (2021) 102903.

[2] N. Kharghani, C. Guedes Soares, Mechanical properties evaluation of the components of a failed hybrid steel-FRP balcony overhang in ships, Mar. Struct. 68 (2019) 102647.

[3] S.A. Hashim, Adhesive bonding of thick steel adherends for marine structures, Mar. Struct. 12 (6) (1999) 405–423.

[4] M. Heshmati, R. Haghani, M. Al-Emrani, Durability of bonded FRP-to-steel joints: Effects of moisture, de-icing salt solution, temperature and FRP type, Composites B 119 (2017) 153–167.

[5] M. Fotouhi, M. Saeedifar, S. Sadeghi, M. Ahmadi Najafabadi, G. Minak, Investigation of the damage mechanisms for mode I delamination growth in foam core sandwich composites using acoustic emission, Struct. Health Monit. 14 (3) (2015) 265–280.

[6] S.-C. Woo, T.-W. Kim, High strain-rate failure in carbon/Kevlar hybrid woven composites via a novel SHPB-AE coupled test, Composites B 97 (2016) 317–328.

[7] M. Saeedifar, M.N. Saleh, P. Nijhuis, S.T. de Freitas, D. Zarouchas, Damage assessment of a titanium skin adhesively bonded to carbon fiber–reinforced plastic omega stringers using acoustic emission, Struct. Health Monit. (2021) 14759217211001752.

[8] M. Saeedifar, D. Zarouchas, Damage characterization of laminated composites using acoustic emission: A review, Composites B 195 (2020) 108039.

[9] E.Ç. Kavdir, M.D. Aydin, The experimental and numerical study on the mechanical behaviours of adhesively bonded joints, Composites B 184 (2020) 107725.

[10] M. Mehrabian, R. Boukhili, 3D-DIC strain field measurements in bolted and hybrid bolted-bonded joints of woven carbon-epoxy composites, Composites B 218 (2021) 108875.

[11] M. Kashfuddoja, M. Ramji, Whole-field strain analysis and damage assessment of adhesively bonded patch repair of CFRP laminates using 3D-DIC and FEA, Composites B 53 (2013) 46–61.

[12] F.N. Ribeiro, M. Martinez, C. Rans, Evaluation of mode II fatigue disbonding using central cut plies specimen and distributed strain sensing technology, J. Adhes. 95 (4) (2019) 259–285.

[13] A. Datta, M.J. Augustin, K.M. Gaddikeri, S.R. Viswamurthy, N. Gupta, R. Sundaram, Damage detection in composite aircraft wing-like test-box using distributed fiber optic sensors, Opt. Fiber Technol., Mater. Devices Syst. 66 (2021) 102651.

[14] M. Saeedifar, M.N. Saleh, ST. De Freitas, D. Zarouchas, Damage characterization of adhesively-bonded Bi-material joints using acoustic emission, Composites B 176 (2019) 107356.

[15] M.N. Saleh, M. Saeedifar, D. Zarouchas, S.T. De Freitas, Stress analysis of double-lap bi-material joints bonded with thick adhesive, Int. J. Adhes. Adhes. 97 (2020) 102480.

[16] P. Xu, Z. Zhou, T. Liu, A. Mal, Determination of geometric role and damage assessment in hybrid fiber metal laminate (FML) joints based on acoustic emission, Compos. Struct. (2021) 270.

[17] P. Xu, Z. Zhou, T. Liu, S. Pan, X. Tan, In-situ damage assessment of FML joints under uniaxial tension combining with acoustic emission and DIC: Geometric influence on damage formation, Thin-Walled Struct. 170 (2022) 108515.
[18] A. Dia, L. Dieng, L. Gaillet, P.B. Gning, Damage detection of a hybrid composite laminate aluminum/glass under quasi-static and fatigue loadings by acoustic emission technique, Heliyon 5 (3) (2019) e01414.
[19] A. International, ASTM E976–10, Standard Guide for Determining the Reproducibility of Acoustic Emission Sensor Response, ASTM International, West Conshohocken, PA, 2010.
[20] R. Hill, A theory of the yielding and plastic flow of anisotropic metals, Proc. R. Soc. Lond. A (1948) 281–297.
[21] S. Askarinejad, E. Martínez-Pañeda, II Cuesta, N. Fleck, Mode II fracture of an MMA adhesive layer: Theory versus experiment, Eur. J. Mech. A Solids 86 (2021) 104133.
[22] C. Li, E. Nordlund, Experimental verification of the Kaiser effect in rocks, Rock Mech. Rock Eng. 26 (4) (1993) 333–351.